Volume 14
Number 26
5 May 2026
Pages 16231–16926

Journal of Materials Chemistry A

Materials for energy and sustainability

rsc.li/materials-a

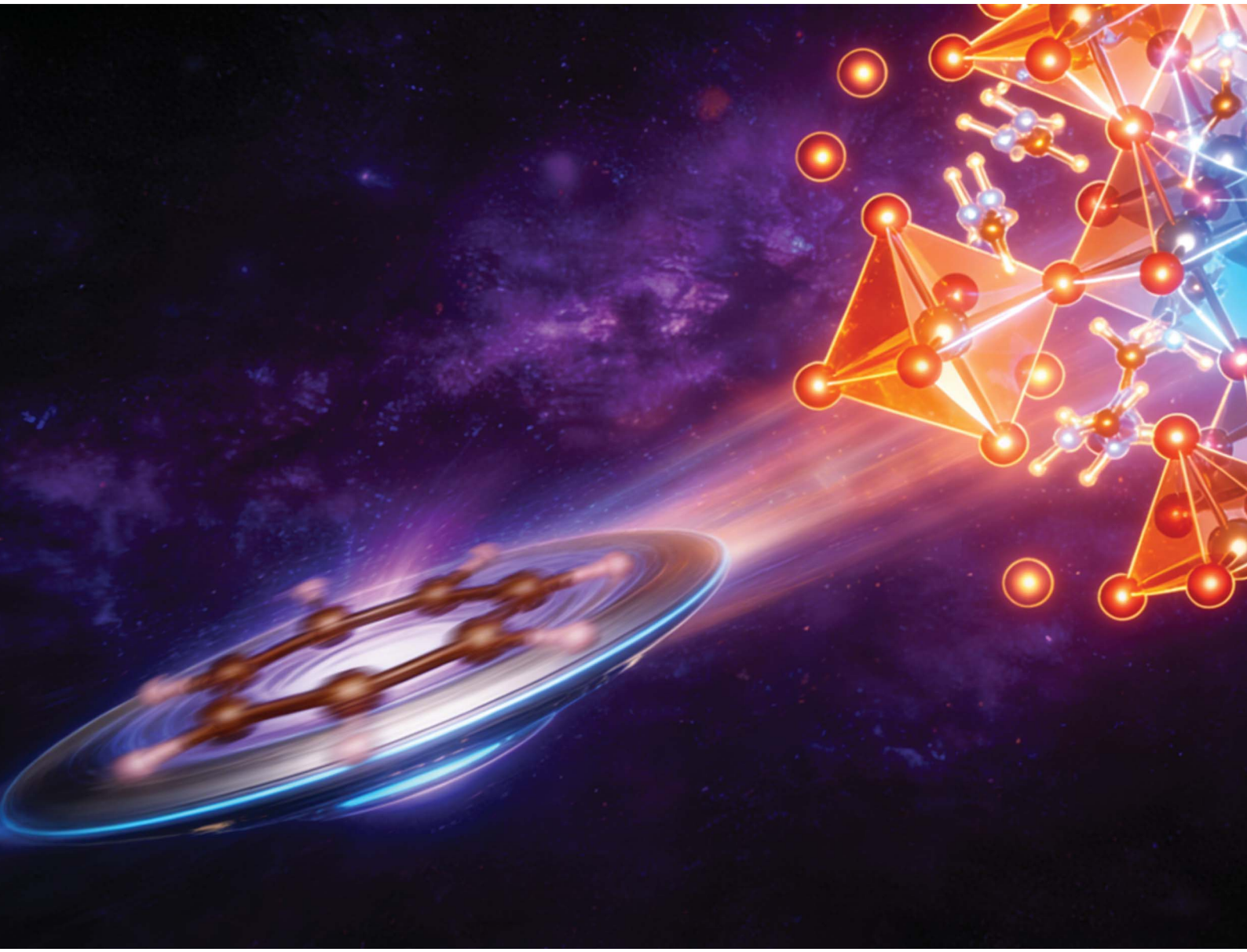

ISSN 2050-7488

ROYAL SOCIETY OF CHEMISTRY

PAPER

Qi Liu and Xiao Cheng Zeng

Quasi-low-dimensional perovskites with enhanced stability against lattice strain and desired band edge by A-site design

Journal of Materials Chemistry A

ROYAL SOCIETY OF CHEMISTRY

PAPER

View Article Online
View Journal | View Issue

Cite this: J. Mater. Chem. A, 2026, 14, 16398

Quasi-low-dimensional perovskites with enhanced stability against lattice strain and desired band edge by A-site design

Qi Liu and Xiao Cheng Zeng *

Quasi-low-dimensional (QLD) additive engineering offers a compelling strategy for stabilizing layered perovskites against lattice strain (Hou *et al.*, *Science*, 2025, **387**, 1069) while tuning the band-edge states. Another recent experiment also demonstrated that the incorporation of charged π-stacking aromatic conjugation (CPAC) A-site cations into the prevailing bulk perovskite for solar cells can lead to reduced bandgaps owing to the strong aromatic polarity of the CPAC cations (Zhu *et al.*, *Nat. Commun.*, 2024, **15**, 2753). In this work, by employing both QLD-additive and CPAC cation design strategies and density-functional theory computation, we examined four CPAC terminal spacers in QLD perovskites: tropylium (Tr), pyridinium (Py), *N*-methylpyridinium (Mp), and *N*-ethylpyridinium (Ep), and the hybrid frameworks of the QLD perovskite stacked with *n*$MAPbI_3$ layers. Our calculation results show that the Tr cation spacer, with the highest aromaticity among the four spacers, leads to the lowest conduction band minimum (CBM) once the Tr-based QLD perovskite is stacked with a multilayer *n*$MAPbI_3$ perovskite. Additionally, as the thickness (*n*) of multilayer *n*$MAPbI_3$ increases, the CPAC spacers with stronger steric hindrance tend to induce phase segregation by lattice strain, leading to irregular band-gap-thickness gradients. Lattice strain resistance analysis indicates that both Tr and Py spacers, benefiting from their relatively strong hydrogen–halogen van der Waals interaction, offer relatively high tolerance to lattice deformation. These theoretical findings suggest that the integration of optimal CPAC spacers in QLD perovskites can be an effective design strategy to enhance structural stability against lattice strain while fine-tuning electronic structures for making durable optoelectronic devices.

Received 3rd January 2026
Accepted 12th March 2026

DOI: 10.1039/d6ta00037a

rsc.li/materials-a

1 Introduction

Perovskite solar cells (PSCs) have attracted considerable attention in the field of photovoltaics due to their remarkable characteristics, including high photovoltaic conversion efficiency (PCE), cost-effectiveness, and simple fabrication processes.[1–3] The first PSC, developed by Miyasaka *et al.*, initially exhibited a modest PCE of 3.8%.[4] To date, ongoing advancements have propelled the certified PCE of single-junction perovskite solar cells beyond 27.3%.[5] Despite notable advancements, several limitations remain for achieving efficient carrier mobility and high chemical stability, optimizing optical absorption across a broad spectral range, and establishing clear relationships between structure and PCE. Tackling these issues is crucial for further improvement in the performance of PSCs.

QLD Ruddlesden–Popper (R–P) layered perovskites have emerged as promising candidates for making solar cells due to their easy-to-realize chemical stability and versatile optoelectronic properties. Structurally, these QLD R–P perovskites consist of inorganic PbI_6^{4-} octahedral layers interspersed with large A-site cation spacers such as phenylethylammonium (PEA, $PhCH_2CH_2NH_3^+$) or butylammonium (BA, $CH_3(CH_2)_4NH_3^+$). The hydrophobic alkyl cations with relatively large spatial hindrance shield the perovskite framework from solvolysis in polar solvents while improving interface charge extraction and reducing surface defects, thereby mitigating degradation deficiencies that often occur in bulk inorganic–organic perovskites.[6–9] Moreover, the energy funneling effect, as demonstrated by Yang *et al.*,[10] can facilitate directional carrier migration due to the bandgap and work-function gradients (induced by the thickness gradient), thereby allowing optical absorption over a broad wavelength range.[10–19] Additionally, compared to their 3D counterparts, QLD R–P perovskites exhibit stronger defect resistance owing to the A-site spacers, thereby achieving longer effective lifetime.[20,21]

However, QLD R–P perovskites still have limitations. The relatively large organic spacers tend to disrupt carrier transport due to the overall localized electronic states and narrowed band dispersions. The large spacers also introduce significant carrier-mobility anisotropy at heterointerfaces of hybrid perovskites, lowering overall device performance. To address these limitations, charged π-stacking aromatic conjugation (CPAC) has emerged as a promising strategy for designing effective spacers

Department of Material Science and Engineering, City University of Hong Kong, Hong Kong SAR 999077, China. E-mail: xzeng26@cityu.edu.hk

that can lead to suitable band structures for the QLD perovskites. A CPAC structure typically involves one or more charged aromatic rings, for example, protonated pyridines (Py^+, $C_5H_5NH^+$) or deprotonated cyclopentadienes (Cp^-, $C_5H_5^-$). Theoretically, density-functional theory (DFT) calculations have predicted that CPAC spacers such as pyridiniums can yield enhanced electronic delocalization and a downshift of the conduction band minimum (CBM), thereby broadening the light absorption range.[22–28] These theoretical predictions have been confirmed by recent experiments. For example, Yu *et al.* showed that their air-fabrication perovskite cells with ionic liquid containing pyridinium salts can yield a high PCE of 25.11%. Also, the moisture-resistance effect of pyridinium cations and their Quat (quaternary ammonium salt) derivatives have been confirmed by experiments.[29–33] A stronger CPAC ring system can even give rise to higher PCE. Recently, Zhu *et al.*[34] designed a QLD perovskite ($MVPb_2I_6$) containing intermolecularly coupled "paraquat" CPAC cations and showed that such a CPAC-based QLD perovskite can suppress interfacial non-radiative recombination and improve carrier extraction. Notably, $MVPb_2I_6$ can yield a high PCE of 25.66% with 95% efficiency retention over 1000 hours. Neilson *et al.*[35,36] successfully synthesized a series of 1D linear perovskites containing an aqua-solution stable CPAC carbocation, tropylium ($C_7H_7^+$, or approx. Tr^+ in this article) with linear MI_6 ($M = Sn^{4+}$, Pb^{2+}, Bi^{3+}, and Sb^{3+}) frameworks, and they achieved narrow-bandgap QLD perovskites with a broadened absorption range in the visible spectra.

Electronic structures in bulk perovskites are susceptible to external strains. Theoretical predictions indicate that a 5% lattice strain can induce marked band distortion, leading to a transition from a direct to an indirect bandgap.[37–42] Also, phase segregation frequently occurs spontaneously in mixed-composition perovskites under various strains. Such strain-induced phase segregation can generate various molecular intermediates, leading to structural defects such as grain boundaries.[43] QLD R–P perovskites, however, can exhibit stronger resistance to lattice strain compared with their 3D analogs.[44–46] Hou *et al.* reported that 2D perovskite coating can enhance lattice stability and suppress light-induced lattice expansion, a common issue in bulk perovskites.[47] Our previous theoretical studies have also shown that 2D coating can stabilize highly active phosphonium perovskite frameworks such as $MPSnBr_3$.[48] Note that while bulky organic cations contribute to structural stability, they tend to incur highly localized bands near the Fermi level and restrict charge carrier migration. As a result, QLD perovskite-based solar cells often exhibit lower PCE than their 3D counterparts.[16] To mitigate these limitations, terminal spacers with good strain-resilience and suitable bandgaps are required for the design of more efficient and stable QLD perovskites.

In this work, we systematically investigated a series of layered QLD perovskites, namely $A_2PbI_4 \cdot n MAPbI_3$, incorporating various CPAC A-site spacers, including protonated pyridine (Py, $C_5H_5NH^+$), *N*-methylpyridinium (Mp, $C_5H_5N–CH_3^+$), *N*-ethylpyridinium (Ep, $C_5H_5N–C_2H_5^+$), and tropylium (Tr, $C_7H_7^+$). Here, the number of $MAPbI_3$ filling layers (n) was varied from 0 to 4. Density-functional theory (DFT) calculations were employed to predict the geometric and electronic structures of these QLD perovskites. Our results show that bulky CPAC spacers can introduce strong steric effects that result in rearrangement of the PbI_6^{4-} octahedral framework with increasing layer number (n). Such steric effects could trigger phase segregation and yield irregular band-gap-thickness relations, in contrast to non-CPAC spacers such as PEA and BA. Furthermore, structural responses to externally applied strain were examined, highlighting distinct deformation behaviors modulated by the CPAC spacers. The overarching aim of this study is to elucidate how CPAC-induced structural perturbation modifies the overall electronic properties and enhances strain resistance of QLD perovskites. By establishing a mechanistic understanding and by proposing a representative model sequence of CPAC-based perovskites, this work provides the groundwork for future experimental validation and potential utilization of these newly predicted materials in high mobility or high strain-resilient optoelectronic devices.

2 Computational methods

First-principles DFT calculations were performed with the Vienna *Ab Initio* Simulation Package (VASP 6.4)[49–51] to compute the geometric and electronic structures of all the bulk and QLD perovskites considered in this work, as well as their heterojunctions with a charge transfer layer. The projector augmented wave (PAW) pseudopotentials with a cutoff energy of 600 eV were employed. The generalized gradient approximation (GGA) exchange–correlation functional, Perdew–Burke–Ernzerhof (PBE), together with the DFT-D3 dispersion correction method of Grimme with zero-damping,[52–54] was applied to optimize the geometrical structures. During the structural optimization, all atoms were allowed to relax until every atom reached mechanical equilibrium without any residual force $>10^{-4}$ eV Å^{-1}.

To compute the electronic structures of the perovskites, the more accurate HSE06 functional was used, as it includes a fraction of screened Hartree–Fock (HF) exchange to improve the discontinuity associated with the derivative of the Kohn–Sham potential at integer electron numbers. Here, the HF exchange parameter $\alpha = 0.38$ was chosen so that our DFT calculation results are closer to the experimental data. For the non-CPAC benchmark, PEA, the default HF exchange parameter $\alpha = 0.2$ was kept. Additionally, the spin–orbit coupling (SOC) effect was accounted for (due to the presence of the heavy atom Pb in the perovskites) in all DFT calculations except geometrical optimization. More specifically, we calculated the partial density of states (pDOS) and optical absorption data of MV $[PbI_3]_2$ (ref. 24) at the HSE06+SOC level of theory to reproduce the experimentally measured band-gap width (see SI Fig. S1). The electronic constituents were 6s 5d 6p for Pb, 5p 6s for I, 5p 6s 4f for Cs, 2s 2p for C and N, and 1s for H. For all the calculations on QLD perovskite slab systems, a 25 Å vacuum layer was adopted so that the spurious interaction among z-direction periodic images would be negligible. All the QLD perovskite slabs were confirmed to be neutral, and the isolated spacer salts were calculated with their counter ions (I^-), as in their relevant

form under experimental conditions. To further reduce any residual periodic-image effects associated with the organic spacers, a 2 × 2 supercell was used for property calculations. Also, for all the QLD systems, we adopted the Monkhost–Pack scheme of 4 × 4 × 1 gamma-centered *k*-point grid for self-consistent calculation. For computing the band structures, we generated the linear sequences of high-symmetry points (20 *k*-points per range) within every lattice vector.

Aromaticity of the spacers was assessed by calculating nucleus-independent chemical shift (NICS) values.[55–57] NICS calculations were carried out by using the ORCA 6.1.1 package[58–63] at the B3LYP[64] level of theory along with the gauge-including atomic orbital (GIAO)[65] method. The def2-TZVP basis[66] set was employed for all atoms. Specifically, NICS values of NICS(1), defined at 1.0 Å above the ring center along the ring normal, were calculated using geometries extracted from the optimized spacer salts.

3 Results and discussion

3.1 Structural and stability of LD CPAC-based A_2PbI_4 perovskites

We considered four CPAC spacers, including pyridiniums—protonated pyridine (Py), *N*-methylpyridium (Mp), and *N*-ethylpyridinium (Ep)—as well as a stable carbocation-bearing species, tropylium (Tr).[25,26] The conventional non-CPAC terminal cation, phenylethylammonium (PEA), was also considered as a benchmark for comparison. The optimized geometric data of all spacers are shown in Fig. S2. The Mp and Ep cations share a similar geometric structure to PEA, but their nitrogen atom with a positive charge is integrated into the aromatic ring (analogous to Py[21,23,40] and MV[24]), leading to a polarized aromatic ring structure with nonuniform charge delocalization. In contrast, the Tr cation exhibits uniform charge delocalization across its seven-carbon tropylium ring (similar to the cyclopentadienyl anion), endowing it with exceptional charge transfer capability.

The optimized spacer cations and LD perovskite layers—Py_2PbI_4, Mp_2PbI_4, Ep_2PbI_4, Tr_2PbI_4, and PEA_2PbI_4 (for benchmark)—are shown in Fig. 1. These QLD perovskites possess

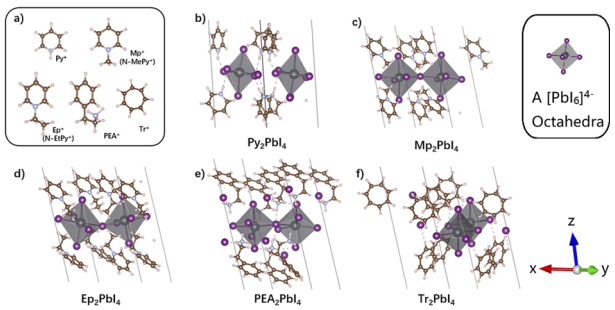

Fig. 1 (a) Optimized spacer cations (CPAC and PEA for benchmark) and (b–f) low-dimensional perovskites with various spacers. The optimized supercells are shown in Fig. S3.

elongated PbI_6^{4-} octahedra along the *z*-axis, which are induced by the insertion of the bulky CPAC spacers. As shown in Table 1, in general, the structure of A_2PbI_4 perovskites highly depends on the molecular geometry of the A-site cations. Flat pancake-like spacers such as pyridinium (Py) and tropylium (Tr) with large Φ_A (diameter) values, tend to form linear, face-sharing 1D structures.[25,40] In contrast, Ep, Mp, and PEA spacers can stabilize 2D arrangements with two face-sharing and one vertex-sharing Pb–I layers due to their polar characteristics and small steric side chains that can be inserted into the PbI_6^{4-} frameworks.

Intermolecular interactions can further differentiate these QLD perovskite systems in terms of the influence of the A-site cation spacer on the stability against lattice strain and the band edge state. Since Py and PEA possess polarized N–H bonds that can have close van der Waals contact with surface iodides (2.40–2.47 Å), more negative formation energies are resulted, indicating stronger binding between surface iodide and the H^+ donor. Although Tr lacks a high-electronegativity H^+ donor (such as $-NH_3^+$ or $=N^+H-$), its π-delocalized charge is distributed over all the ring carbons, enabling weaker but still stable van der Waals contact (2.91 Å; $E_{form} = -90.04$ meV) that can provide modest resistance to lattice strain. In contrast, the quaternized pyridinium cations (Ep and Mp) lack H^+ donors, and they interact primarily with terminal iodides *via* coulombic attraction, resulting in relatively longer vertical Pb–I distances (3.36–3.39 Å) and less negative formation energies. In particular, Mp ($E_{form} = -28.35$ meV per atom) results in lower stability due to the short alkyl substituent. The latter allows deeper pyridine insertion that can disrupt Pb–I bonding. Such structural distortions can also localize hole states near the valence band maximum (VBM), likely reducing carrier mobility. In Fig. 2, the computed electronic structures, including the bandgaps at different levels of theory, effective carrier masses, and optical absorption spectra, are shown. The detailed pDOSs are shown in Fig. S4. As shown in Fig. 2a, all CPAC-based QLD perovskites exhibit reduced bandgaps, compared to the ring-uncharged PEA-based structure (benchmark), thereby enhancing visible light absorption and facilitating charge transfer. Among the pyridinium-based cation species (Py, Mp, and Ep), the bandgap decreases as the *N*-alkyl chain length increases. Notably, the Tr-based perovskite has the narrowest bandgap due to the extended conjugation across seven carbon atoms, effectively lowering the CB edge.

It is known that carrier transport is strongly dependent on carrier's effective mass.[67–71] The effective masses of carriers for the CPAC-based LD perovskites were determined by fitting the energy dispersions of the VB and CB edges to quadratic functions, *i.e.*, $\frac{1}{m_{ii}^*} = \frac{1}{\hbar}\frac{\partial^2 E_n(\kappa_i)}{\partial {\kappa_i}^2} (i = x, y)$, where m_{xx}^* and m_{yy}^* correspond to the effective mass along the *x* and *y* directions, respectively, and E_n represents the computed band dispersions at the given *k*-point vector (see Fig. S5). Fig. 2b illustrates that all CPAC-based QLD perovskites exhibit higher electron effective masses (m^*) than the corresponding bulk perovskite (benchmark; $0.06m_e$) due to reduced dimensionality. Quat pyridinium-

Table 1 Optimized low dimensional (1D/2D) CPAC perovskites A_2PbI_4 and computed formation energies. Here, the bracketed A–I length represents the minimum distance between I^- and the H^+ (proton) donor in the functional group, *e.g.*, H in $-NH_3^+$

Spacers	Py	Mp	Ep	PEA	Tr
Φ_A	2.73	4.23	4.99	5.15	3.26
a	7.55	9.61	8.98	7.80	8.78
b	10.14	10.18	10.17	9.51	10.58
h	12.27	13.28	12.84	16.11	10.89
α	77.89	78.94	77.86	81.56	104.63
β	90.85	94.78	97.41	90.80	81.39
Max d_{Pb-I}/Å	3.38	3.39	3.36	3.32	3.32
Avr. d_{Pb-I}/Å	3.21	3.28	3.26	3.26	3.25
I–Pb–I/deg.	81.6	82.46	87.56	82.83	81.89
d_{A-I}/Å	3.37(2.47)	3.98	4.09	3.38(2.40)	4.66(2.91)
E_{form}/meV per atom	−139.27	−28.35	−77.47	−117.47	−90.04

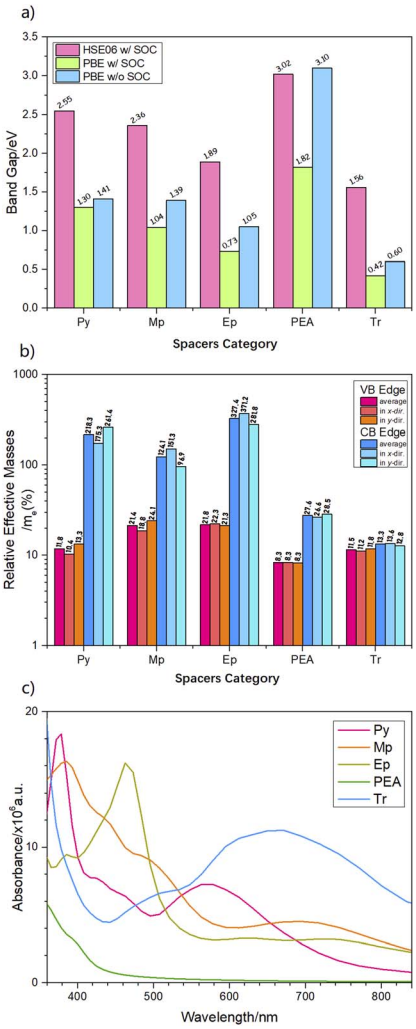

Fig. 2 Computed (a) bandgaps, (b) effective carrier masses, and (c) optical absorption spectra of CPAC-based LD perovskite A_2PbI_4 with different terminal spacers and different levels of theory. Here, "w" denotes "with", and "w/o" denotes "without".

based structures (Mp and Ep) exhibit abnormally large m^* values ($>2m_e$) at the CBM, indicating strong carrier localization with hindered carrier transport, consistent with prediction based on the electronic structures. The effective-mass anisotropy in the x and y directions further suggests slower carrier transport along the y-orientation, limiting overall mobility. Fig. 2c shows the computed optical absorption spectra, where all CPAC-based structures display enhanced absorption in the visible range, compared with PEA_2PbI_4. In particular, Tr_2PbI_4's spectrum extends into the near-infrared region, owing to its narrowed bandgap. The observed redshift in absorption peaks is highly correlated with relatively large pyridinium alkyl length, as well as consistent with the trend predicted based on the bandgaps. Thus, the incorporation of CPAC spacers introduces delocalized CBM states that can improve light harvesting through tunable band edges, thereby addressing inherent optical limitations of QLD perovskites.

To further clarify the relationship between spacer aromaticity and the electronic structure of LD perovskites, we calculated the NICS[55–57] (as NICS(1)) values of the aromatic spacers considered and compared these values with the computed band gaps shown in Fig. 2. As shown in Fig. 3, the band gaps of CPAC-terminated QLD perovskites exhibit an approximately linear

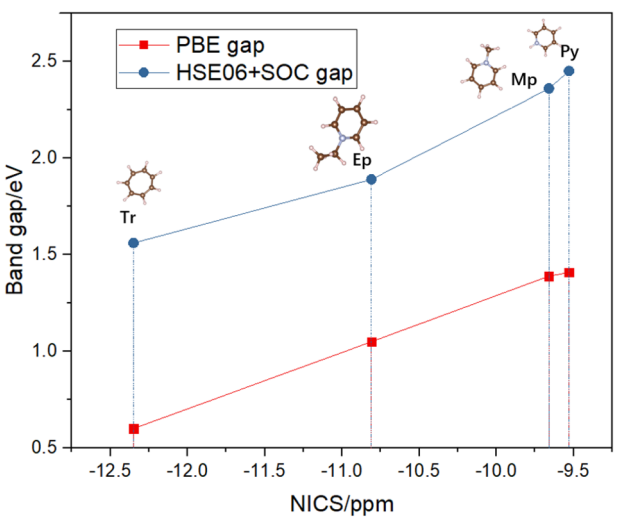

Fig. 3 Calculated band gaps of the LD perovskite layers *versus* NICS (as NICS(1)) of their spacers.

correlation with the NICS values of the corresponding terminal cations. It is worth noting that, although PEA shows a relatively low NICS value (∼−10.3), its band gap is markedly wider than those of CPAC-terminated LD perovskite structures because the positive charge center in PEA does not participate in the extended π-conjugation. These results further support our conclusion that CPAC cations make an effective contribution to the electronic states near the Fermi level in LD perovskites, and that stronger aromatic conjugation enables deliberate and quantitative tuning of the band gap.

3.2 Structural stability of QLD CPAC-based A_2PbI_4 perovskites

Next, we theoretically designed QLD R–P perovskite frameworks, aiming to achieve structural flexibility through controlled variation of the layer thickness. The PEA structures were excluded from further consideration, as they do not offer the CPAC effect at their charged ammonium termini. To describe the ordering of PbI_6^{4-} octahedra within the newly designed frameworks, we adopted two abbreviations: (1) "F" denotes face-sharing, and (2) "V" denotes vertex-sharing connectivity. For instance, a 2F-1V sequence indicates a structural motif with two face-sharing octahedra and one vertex-sharing unit. As illustrated in Fig. S6, CPAC-based frameworks with two $MAPbI_3$ layers exhibit cross-linked 2F-1V motifs capped by quasi-linear 1D coatings, reflecting the structural constraints imposed by the bulky spacers. In contrast, the frameworks with three or more stacked layers display parallel 2F-1V sequences, including the terminal layers with spacers. These structural configurations resemble those observed in standard quasi-2D $MAPbI_3$ layered perovskites.

To assess the structural stability of these hybrid layer-stacked frameworks, particularly those involving large spacers, we evaluated their phase-segregation tendencies by computing the reaction energy associated with a net decomposition reaction:

$$A_2PbI_4{\cdot}nMAPbI_3 \rightarrow A_2PbI_4 + (MAPbI_3)_n \quad (1)$$

where the phase-segregation energy is defined as $E_{seg} = E_{QLD} - (E_{A_2PbI_4} + E_{(MAPbI_3)n})$ and n represents the thickness of the $MAPbI_3$ layers. The phase-segregation energy is a measure of the thermodynamic favorability toward surface-layer dissociation, especially in multi-layered structures. It also reflects the limits of structural resilience of CPAC-based layered perovskite frameworks: $A_2PbI_4{\cdot}nMAPbI_3$. The calculated largest Pb–I distance at the surface and segregation energies of various frameworks with different CPAC spacers and n are summarized in Fig. 4, and the detailed geometric parameters are given in Tables S1 and S2. As shown in Fig. 4a, the extended Pb–I bond length reflects weak coupling between CPAC spacers and the inorganic framework, suggesting a tendency for CPAC spacers to detach from the surface by releasing A^+ and I^- ion pairs. An exception is the smallest CPAC spacer, Py, whose H^+ donor engages in stronger van der Waals interaction with the PbI_6^{4-} octahedra, which helps to stabilize the surface. The Tr cation also contains the H^+ donor, but its uniform electron

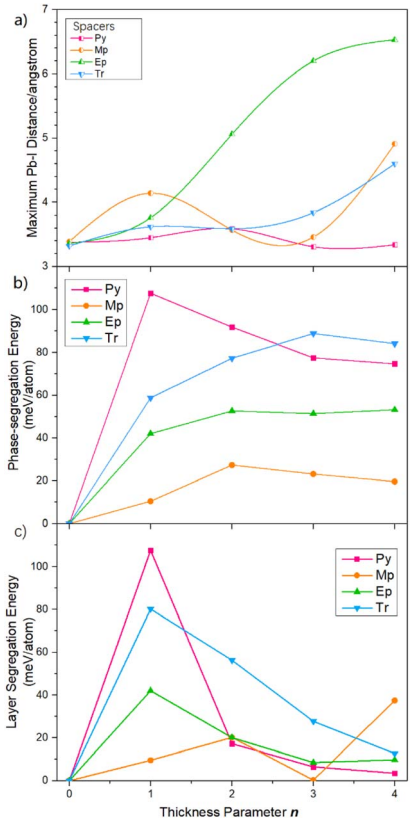

Fig. 4 Computed (a) maximum Pb–I distance at the surface, (b) phase-segregation energy and (c) layer-segregation energy of CPAC-based layered perovskite frameworks ($A_2PbI_4{\cdot}nMAPbI_3$) with different spacers *versus* $MAPbI_3$ layer thickness n.

delocalization lowers the overall polarity, weakening the van der Waals interaction while slightly increasing the Pb–I bond length.

The phase segregation is more likely to occur in the case of quat cations such as Mp and Ep due to the absence of H^+ donors and hydrogen bonding (see Fig. 1, S3 and S6). Additionally, the bulky size of the quat cations and their strong electrostatic interaction can further distort the PbI_2-terminated surface structure. In particular, $Ep_2PbI_4{\cdot}nMAPbI_3$ ($n > 3$) shows considerable detachment of isolated EpI and $MAPbI_3$ species due to Ep's large size with the longest maximum Pb–I distance up to 6 Å among all cations considered.

As depicted in Fig. 4b and Table S4, the phase-segregation energies increase sharply when CPAC-based QLD perovskite layers form heterojunctions with $MAPbI_3$, particularly in Py_2PbI_4 and Tr_2PbI_4, where H^+ donors alter the octahedral connectivity at terminal interfaces. With increasing $MAPbI_3$ thickness (n), the segregation energies gradually decrease, indicating higher thermodynamic favorability for phase segregation. This trend reflects both the diminished impact of van der Waals interaction on the stability, and the growing mismatch between the QLD spacer surface and the $MAPbI_3$ interlayers. Notably, for $n > 3$, segregation energies converge across all CPAC-based frameworks, suggesting that beyond $n = 3$, the CPAC-based QLD perovskite structures approach a bulk-

like $MAPbI_3$ structure. The interfacial mismatch between the CPAC-based QLD perovskite structure and $MAPbI_3$ enhances the likelihood of phase segregation toward separated A_2PbI_4 and $MAPbI_3$ domains. Given the reduced structural influence of CPAC spacers beyond $n = 3$, we will not consider strain-induced electronic effects for $n > 3$.

Fig. 4c and Table S5 display the calculated layer segregation energy, which represents the opposite of the interlayer binding energy, as:

$$A_2PbI_4{\cdot}nMAPbI_3 \rightarrow A_2PbI_4{\cdot}(n-1)MAPbI_3 + MAPbI_3\ (n = 1\ \text{to}\ 4) \quad (2)$$

Among the QLD perovskite structures, the Py cation exhibits the strongest ability to suppress layer segregation. However, since only the N–H group can form hydrogen bonds (bond length: 2.41 Å), its stabilization effect *via* hydrogen bonding imposes certain constraints on the arrangement and orientation of the lead iodide octahedra. As the number of perovskite layers increases, the hydrogen-bonding stabilization is partially suppressed due to the reorientation of the pyridine nitrogen.

In contrast, the Tr cation features uniform π-delocalization, rendering all seven hydrogens on its ring equivalent and capable of forming hydrogen bonds. Consequently, it behaves more uniformly with increasing perovskite layer count, a trend that stands in clear contrast to the Py-capped perovskites. Furthermore, since the hydrogen bonds formed by Tr are weaker (bond length: 2.91 Å), the maximum layer segregation energy of Tr-capped perovskites is lower than that of Py-capped ones. Owing to the absence of polar hydrogen atoms, Mp and Ep cations generally exhibit lower resistance to layer segregation.

The overall structural modifications, including elongated Pb–I distance, surface polarization, and interface mismatch, can alter the electronic structure of QLD perovskites. Variations in CPAC terminal species and layer thickness (n) can result in systematic bandgap shifts and different optical responses, underscoring a tight coupling between the interfacial structure and electronic behavior of these hybrid frameworks. The calculated n-dependent bandgaps are presented in Fig. 5, and orbital-level insights provided by pDOS are shown in Fig. S7–S10.

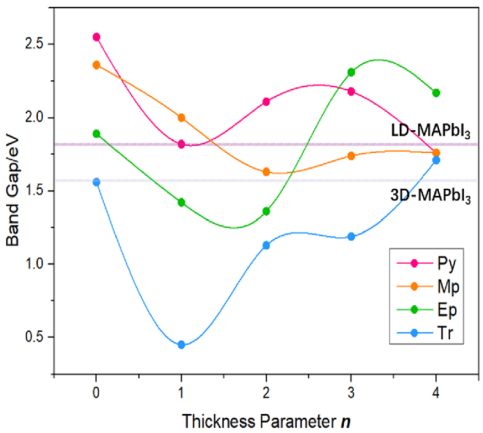

Fig. 5 Computed bandgaps of multilayer R–P CPAC-based perovskite $A_2PbI_4{\cdot}nMAPbI_3$ with different spacers, at the HSE06+SOC level of theory. The horizontal purple lines show the 3D and QLD structures of pure $MAPbI_3$ for comparison.

The pDOS indicates that CPAC-based QLD perovskites are still dependent on n. However, due to the low CB edge and strong steric hindrance of CPAC spacers, the pDOS dependence of n deviates markedly from the linear trend typical of PEA- or BA-based systems.[10,14,16–18,72] As illustrated in Fig. 4, the bandgap initially decreases as n increases from 0 to 1, regardless of the structure of spacers. This band-gap reduction can be attributed to the enhanced connectivity within the $[PbI_6]^{4-}$ octahedral framework, facilitated by the cross-linking effect of $MAPbI_3$. For CPAC spacers with H^+ donors such as Py and Tr, the substantial lattice mismatch between the flat spacers and the 3D $[PbI_6]^{4-}$ framework results in a large reduction of bandgap from $n = 0$ to $n = 1$. The calculated band structures (see Fig. S11) confirmed this result. This is primarily due to steric incompatibility that weakens the internal Pb–I interaction and elevates the VB edge. For Tr-based structures, the stronger CPAC effect further downshifts the CB edge to a minimum of 0.84 eV, thereby enhancing optical absorption capability towards the visible and near-infrared regions.

For quat spacers such as Mp and Ep, the absence of H^+ donors, together with their significant steric hindrance, leads to enlarged spatial separation between the positively charged centers and neighboring iodide ions in CPAC-based QLD perovskites, particularly for $n = 1$–2. Beyond $n = 2$, the bandgap of the CPAC-based QLD perovskites starts to increase gradually with n and eventually converges to an asymptotic value, a characteristic of layered $MAPbI_3$ with a 2F-1V octahedral stacking sequence (see Fig. S12), independent of the CPAC type. This convergence suggests that the inductive and steric effects of CPACs on the $[PbI_6]^{4-}$ framework become diminished for $n > 3$. Among the cations considered, Ep is the most destabilizing one, since its large steric demand tends to promote strong phase segregation for $n > 3$, as reflected by the reduced cross-linked structures of the Pb–I network and increased bandgaps. These results confirm that the CPAC spacers are very effective for engineering band edges of multilayer heterostructures ($n < 3$), where their steric and electronic interactions remain strongly coupled with the PbI_6^{4-} framework. Beyond $n = 3$, their influence diminishes, and the electronic structure becomes increasingly dictated by the bulk $MAPbI_3$ properties.

3.3 How do CPAC-based QLD perovskites with H^+ donors show good strain resilience

QLD layered perovskites are often subjected to spontaneous strain tension under various external conditions.[45–47] To further understand this behavior, the strain response of CPAC-based QLD perovskites under different degrees of biaxial strain were investigated. As aforementioned, for structures with $n \geq 3$, the influence of terminal CPAC spacers becomes minimal. Thus, in this section, we focus only on QLD configurations with $n = 0$–2. The calculated deformation energies and the maximum surface Pb–I bond length under various biaxial strains (−5% and −2%

as compression, and +2% and +5% as extension) are shown in Fig. 5, while more detailed data are shown in Tables S6 and S7. Here, the strain is given by:

$$\varepsilon_{\text{deform}} = \frac{E_{\text{strain}} - E_{\text{pristine}}}{N} \quad (3)$$

where $\varepsilon_{\text{deform}}$ represents the deformation energy, E_{strain} is the energy of a layered QLD structure under biaxial strain, E_{pristine} represents the energy without strain (see Table 1 and S7), and N represents the thickness of the $MAPbI_3$ stacked layers. In the QLD perovskite structures, spacers such as Tr and Py have the highest resistance to deformation due to their tensed 1D-linear connectivity. The deformation energy of Py was found to be higher than that of Tr, attributed to the polarity of the Py cation. Specifically, the iodide anion interaction—arising from van der Waals forces between the polar hydrogen of Py and the perovskite surface—shows a shorter H–I distance (2.58 Å) compared to Tr (2.91 Å).

Furthermore, in the case of a single $MAPbI_3$ layer ($n = 1$), an intermediate conformation forms between the 1D linear $(Py/Tr)_2PbI_4$ and the 3D cross-linked cubic lattices. This intermediate structure weakens the Pb–I interactions, increases the structural distortion, and ultimately results in a lower deformation energy. This observation aligns with previous discussion without strain-induced deformation. Nevertheless, for the hybrid perovskite structure of QLD $A_2PbI_4 \cdot n MAPbI_3$, the slightly thicker $n = 2$ structure still exhibits lower strain tolerance than the rigid monolayer structure ($n = 0$), despite possessing a higher deformation energy than the well-characterized reference pure-phase perovskite (*e.g.*, $[FACs]_{0.5}PbI_3$ in Fig. S15),[47] except in the cases of large strain of +5%. The monolayer perovskite Tr_2PbI_4 shows a strong deformation tendency toward phase segregation under compressive strain (see Fig. 6b and Tables S6, S7) due to its relatively large and flat size with low polarity, which gives rise to a large deformation energy (Fig. 6a). However, the nMAPbI$_3$-layer ($n \geq 1$) stacked QLD structures maintain the 3D linkage among various layers with the reorientation of the spacers (see Fig. S13–S16).

Due to the absence of H^+ donors, quat spacers such as Mp and Ep lack van der Waals interaction generated by the H^+ donor and $[PbI_6]^{4-}$ frameworks. As a result, the structures of $n = 0$ have fragile 2D planes with lower deformation energies. Incorporating $MAPbI_3$ stacked layers can enhance strain resistance through increased van der Waals coupling between MA cations and the $[PbI_6]^{4-}$ framework. Moreover, as presented in Fig. 6b and Table S7, structures that include Ep and Mp spacers show a pronounced increase in surface Pb–I distance ($d_{(Pb-I)}$) under compression, indicating structural instability and a higher tendency for phase segregation.

We also investigated the strain-induced electronic responses for the QLD perovskites with various spacers. The calculated bandgaps are summarized in Fig. 7, while detailed numerical values of the bandgaps and electronic density of states at various strains are given in Table S8 and Fig. S18–S21, respectively. For perovskites terminated with spacers containing H^+ donors (Py and Tr), the bandgap shows systematic increases under tensile strain and decreases under compressive strain. This trend is consistent with that predicted based on the geometric deformation of the PbI_6^{4-} octahedral framework, with its structural coherence being largely maintained until phase segregation occurs. For instance, Py-based structures with $n = 0$ display a trend of bandgap increase from 1.99 eV at −5% to 2.54 eV at +5% strains, while Tr-based analogues display a trend of bandgap increase from 1.21 eV to 1.69 eV across the same range of strains.

By contrast, structures terminated with quat spacers (Mp and Ep) demonstrate a notably different response due to the absence of van der Waals interactions between the quat cations and the PbI_6^{4-} framework. At $n = 0$, their bandgaps remain relatively wide (*e.g.*, 2.17–2.43 eV for Mp), or behave irregularly under strain, reflecting partial segregation within the isolated spacer salts (MpI/EpI) and $[PbI_6]^{4-}$ networks. These structures display limited strain tolerance and are prone to phase segregation, particularly under compressive strains. The phase segregation, if it occurred, would lead to the formation of Q2D $MAPbI_3$ cubic layers with limited contribution from the terminal CPAC spacers. Consequently, a sharp increased bandgap is resulted, indicating the disruption of electronic coupling with respect to the strain-free structures and the

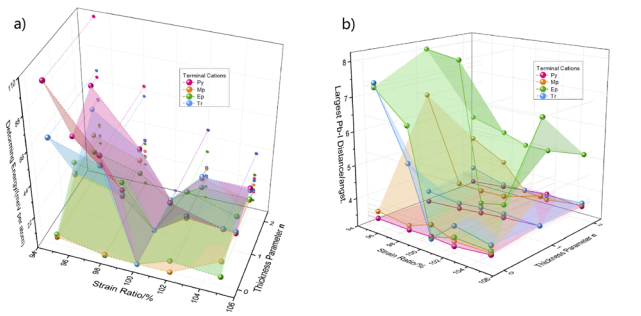

Fig. 6 Computed (a) deformation energy (in meV per atom) and (b) the longest surface Pb–I distance (max. d_{Pb-I}) in multilayer CPAC-based perovskite $A_2PbI_4 \cdot n MAPbI_3$ ($n = 0$ to 2) with different spacers at various strains. Detailed numerical data are given in Tables S6 and S7. The data of $(FACs)_{0.5}PbI_3$ can be used as a comparative reference (see Fig. S17).

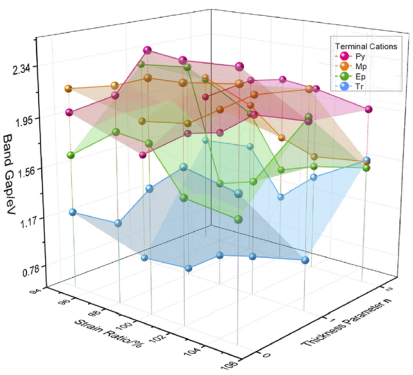

Fig. 7 Computed bandgaps of multilayer R–P CPAC-based perovskites: $A_2PbI_4 \cdot n MAPbI_3$ ($n = 0$–2) with different spacers at various strains. DFT computation is at the theory level of HSE06+SOC. Detailed numerical data are given in Table S8.

reduced dimensionality of the perovskite framework. Overall, a consistent trend across all spacer types is that the $n = 1$ perovskite frameworks have the smallest bandgaps, irrespective of the external strain. This result suggests that the structures with modest thickness can retain optimal orbital overlap and lattice flexibility under mechanical perturbation, rendering them particularly favorable for tuning the bandgap in strain-engineering applications.

4 Conclusions

The nature of organic A-site cations plays a critical role in determining the optoelectronic characteristics of layered perovskites. The present study demonstrates that the organic CPAC spacers can have profound influence on the optoelectronic properties of QLD layered perovskites to evaluate how variations in terminal cation chemistry influence band gap behaviour, carrier effective mass, and optical absorption performance.

Our results demonstrate that the incorporation of charged aromatic rings significantly reduces the conduction band minimum (CBM), thereby narrowing the intrinsic wide band gap of conventional LD perovskites. This reduction follows the trend Tr > Ep > Mp > Py > PEA (as non-CPAC benchmark), correlating with the degree of delocalization in the charged aromatic heterocycles (inferred from NICS values). Notably, tropylium-terminated structures exhibit band gaps even lower than bulk $MAPbI_3$, expanding photo response into the visible and near-infrared regions—an advantageous trait for light-harvesting applications.

From a structural standpoint, the layered configurations show different tendencies to form QLD layered structures with $MAPbI_3$ layers. Although all QLD CPAC-based perovskites tend to phase segregate at thicknesses beyond $n = 3$ and release isolated spacer salts (PyI, TrI, MpI and EpI), this tendency can be suppressed by the van der Waals interaction provided by H^+ donors. In particular, Py and Tr spacers demonstrate enhanced interlayer cohesion due to van der Waals interaction with iodide anions, thereby suppressing the tendency of phase segregation while keeping structural integrity. In contrast, quat spacers, *e.g.*, Mp and Ep, which lack H^+ donors and have a large steric mismatch with the PbI_6^{4-} framework, tend to promote phase/layer segregation and are therefore less suitable for stable multilayer assembly.

The mechanical-strain response further highlights these distinctions. Py and Tr cations, due to their dipole moments and van der Waals interactions, exhibit superior tolerance to compressive strain. However, Tr's larger molecular diameter leads to compression-induced instability in monolayer configurations. On the other hand, quat cations Mp and Ep, dominated by electrostatic rather than dispersive interactions, show a strong propensity for phase separation under compression, as indicated by abrupt band gap shifts and low separation energies. Nonetheless, these QLD structures demonstrate notably high tolerance to tensile strain, offering potential utility for applications in mechanical deformation or lattice mismatch engineering.

The molecular-level insights gained from this study of substituting CPAC spacers in QLD perovskites will benefit future design of perovskite-based devices with structure flexible and light-harvesting features, as well as anisotropic charge transport potential and tunable mechanical resilience.

Author contributions

Q. Liu designed and operated the DFT computational research and wrote the article. X. C. Zeng supervised the project. All the authors have reviewed the article file.

Conflicts of interest

There are no conflicts to declare.

Data availability

The data supporting this article have been included as part of the supplementary information (SI). Additional data that support the findings of this study are available from the corresponding author upon reasonable request. Supplementary information: optimized geometries, HSE06+SOC band structures, and projected densities of states (pDOS) for and Pb (A = Py, Mp, Ep, PEA, and Tr). Geometric parameters, total energies, and pDOS for layer-stacked Pb·*n*MAPb (A = Py, Mp, Ep, and Tr; $n = 1$–4), together with bulk MAPb as a reference. Complete band-structure plots for Pb·*n*MAPb (A = Py, Mp, Ep, and Tr). Optimized strained geometries and corresponding pDOS for Pb·nMAPb (A = Py, Mp, Ep, and Tr; $n = 0$–2). Numerical data associated with the 3D plots are provided in Tables S5–S7. See DOI: https://doi.org/10.1039/d6ta00037a.

Acknowledgements

X. C. Z. acknowledges the support from the Hong Kong Global STEM Professorship Scheme and the Research Grants Council of Hong Kong Grant (C1055-23 G and CRS Cityu 104/24).

Notes and references

1 A. Jena, A. Kulkarni and T. Miyasaka, Halide Perovskite Photovoltaics: Background, Status, and Future Prospects, *Chem. Rev.*, 2019, **119**, 3036–3103.
2 S. D. Stranks and H. J. Snaith, Metal–Halide Perovskites for Photovoltaic and Light-Emitting Devices, *Nat. Nanotechnol.*, 2015, **10**, 391–402.
3 M. Grätzel, The Light and Shade of Perovskite Solar Cells, *Nat. Mater.*, 2014, **13**, 838–842.
4 A. Kojima, K. Teshima, Y. Shirai and T. Miyasaka, Light Sensitizers for Photovoltaic Cells, *J. Am. Chem. Soc.*, 2009, **131**, 6050–6051.
5 National Renewable Energy Laboratory, *Best Research-Cell Efficiencies*, 2026, available at https://www.nrel.gov/pv/cell-efficiency.
6 R. Ouyang, Exploiting Ionic Radii for Rational Design of Halide Perovskites, *Chem. Mater.*, 2020, **32**, 595–604.

7 T. Chakrabarti, S. Kaarthik and A. Perumal, Phenethylammonium Halide Blend as an Efficient Interlayer in Solution-Processed Inverted Planar p–i–n Perovskite Solar Cells, *ACS Appl. Energy Mater.*, 2025, **8**, 2837–2844.

8 D. Thrithamarassery Gangadharan and D. Ma, Searching for stability at lower dimensions: current trends and future prospects of layered perovskite solar cells, *Energy Environ. Sci.*, 2019, **12**, 2860–2889.

9 X. Li, Y. Fu, L. Pedesseau, P. Guo, S. Cuthriell, I. Hadar, J. Even, C. Katan, C. C. Stoumpos, R. D. Schaller, E. Harel and M. G. Kanatzidis, Negative Pressure Engineering with Large Cage Cations in 2D Halide Perovskites Causes Lattice Softening, *J. Am. Chem. Soc.*, 2020, **142**, 11486–11496.

10 A. M. Oddo, M. Gao, D. Weinberg, J. Jin, M. C. Folgueras, C. Song, C. Ophus, T. Mani, E. Rabani and P. Yang, Energy Funneling in a Noninteger Two-Dimensional Perovskite, *Nano Lett.*, 2023, **23**, 11469–11476.

11 L. N. Quan, M. Yuan, R. Comin, O. Voznyy, E. M. Beauregard, S. Hoogland, A. Buin, A. R. Kirmani, K. Zhao, A. Amassian, D. H. Kim and E. H. Sargent, Ligand-Stabilized Reduced-Dimensionality Perovskites, *J. Am. Chem. Soc.*, 2016, **138**, 2649–2655.

12 M. Yuan, L. Quan and R. E. A. Comin, Perovskite energy funnels for efficient light-emitting diodes, *Nat. Nanotechnol.*, 2016, **11**, 872–877.

13 J. Liu, J. Leng, K. Wu, J. Zhang and S. Jin, Observation of Internal Photoinduced Electron and Hole Separation in Hybrid Two-Dimensional Perovskite Films, *J. Am. Chem. Soc.*, 2017, **139**, 1432–1435.

14 L. Lei, D. Seyitliyev, S. Stuard, J. Mendes, Q. Dong, X. Fu, Y.-A. Chen, S. He, X. Yi, L. Zhu, C.-H. Chang, H. Ade, K. Gundogdu and F. So, Efficient Energy Funneling in Quasi-2D Perovskites: From Light Emission to Lasing, *Adv. Mater.*, 2020, **32**, 1906571.

15 N. Zhou, Y. Shen, L. Li, S. Tan, N. Liu, G. Zheng, Q. Chen and H. Zhou, Exploration of Crystallization Kinetics in Quasi Two-Dimensional Perovskite and High Performance Solar Cells, *J. Am. Chem. Soc.*, 2018, **140**, 459–465.

16 Y. Huang, T. Liu, D. Li, D. Zhao, A. Amini, C. Cheng and G. Xing, Limitations and solutions for achieving high-performance perovskite tandem photovoltaics, *Nano Energy*, 2021, **88**, 106219.

17 X. Liang, *et al.*, Promoting Energy Transfer Between Quasi-2D Perovskite Layers Toward Highly Efficient Red Light-Emitting Diodes, *Small*, 2022, **18**, 2204638.

18 M. Li, Q. Gao, P. Liu, Q. Liao, H. Zhang, J. Yao, W. Hu, Y. Wu and H. Fu, Amplified Spontaneous Emission Based on 2D Ruddlesden–Popper Perovskites, *Adv. Funct. Mater.*, 2018, **28**, 1707006.

19 I. Wagner, W. T. Van Gompel, R. Erkens, B. Ruttens, J. D'Haen, L. Lutsen, D. Vanderzande, C. Chuang, S. H. Chang, P. A. Hume, M. B. Price, P. Geiregat, J. M. Hodgkiss and K. Chen, Critical Roles of Ultrafast Energy Funnelling and Ultrafast Singlet-Triplet Annihilation in Quasi-2D Perovskite Optical Gain Mechanisms, *Adv. Mater.*, 2025, **37**, 2419674.

20 C. M. Perez, D. Ghosh, O. Prezhdo, W. Nie, S. Tretiak and A. Neukirch, Point Defects in Two-Dimensional Ruddlesden–Popper Perovskites Explored with *Ab Initio* Calculations, *J. Phys. Chem. Lett.*, 2022, **13**, 5213–5219.

21 G. Giulia, C. Roldan-Carmona, I. Zimmermann, E. Mosconi, X. Lee, D. Martineau, S. Narbey, F. Oswald, F. De Angelis, M. Grätzel and M. K. Nazeeruddin, One-Year Stable Perovskite Solar Cells by 2D/3D Interface Engineering, *Nat. Commun.*, 2017, **8**, 15684.

22 N. I. Selivanov, Y. A. Rozhkova, R. Kevorkyants, A. V. Emeline and D. W. Bahnemann, The effect of organic cations on the electronic, optical and luminescence properties of 1D piperidinium, pyridinium, and 3-hydroxypyridinium lead trihalides, *Dalton Trans.*, 2020, **49**, 4390–4403.

23 R. Kevorkyants, A. Emeline and D. Bahnemann, Hybrid lead triiodide perovskites with unsaturated heterocyclic cations containing N, O, and S atoms: *Ab initio* study, *J. Solid State Chem.*, 2020, **282**, 121082.

24 N. I. Selivanov, A. A. Murashkina, R. Kevorkyants, A. V. Emeline and D. W. Bahnemann, Pyridinium lead tribromide and pyridinium lead triiodide: quasi-onedimensional perovskites with an optically active aromatic π-system, *Dalton Trans.*, 2018, **47**, 16313–16319.

25 W. Fu, T. Zhao, H. Liu, F. Lin, L. Zuo, X. Li and A. K.-Y. Jen, High-Efficiency Quasi2D Perovskite Solar Cells Incorporating 2,2'-Biimidazolium Cation, *Sol. RRL*, 2021, **5**, 2000700.

26 H. Xu, X. Hu, F. Sun, J. Sun, W. Guo, Y. Liu, W. Liu, X. Fu, J. Luo and Z. Sun, Visible-Photoactive Ferroelectric Semiconductor Incorporating Aromatic Dynamic Spacer Enables Optoelectronic Synaptic Plasticity, *Adv. Mater.*, 2025, **37**, 2504953.

27 Y. Zhou, Y. Zhang, L. Zhang, H. Wu, Y. Zhou, X. Xu, J. Yu, X. Wu, J. Xie, W. Fu, G. Wu and H. Chen, Aromatic Imidazole Diammonium-based 2D Dion-Jacobson Perovskites with Reduced Exciton Binding Energy, *Adv. Funct. Mater.*, 2024, **34**, 2408774.

28 Y. Liu, J. Guo, H. Zhou, C. Li and X. Guo, Correlating π-pi Stacking of Aromatic Diammoniums with Stability and Dimensional Reduction of Dion–Jacobson 2D Perovskites, *J. Am. Chem. Soc.*, 2024, **146**, 8198–8205.

29 S. Tang, Y. S. Gou, C. Deng, C. L. Yuan, P. Zhao, C. Li, J. Y. Chen, H. M. Li and H. Yu, Optimized Crystallization via Ionic Liquid Engineering for Air-Fabricated Perovskite Solar Cells with Efficiency of 25.11%, *Solar RRL*, 2025, **9**, 2500104.

30 J. Cha, C. Beom Lee, S. Min Park, D. Baek and S. Kim, Lattice-matched insitu-formed 1D perovskite phase in Multi-dimensional solar cells achieving high phase stability and favorable energy landscape, *Chem. Eng. J.*, 2024, **484**, 149280.

31 X. Jiang, L. Zhu, B. Zhang, G. Yang, L. Zheng, K. Dong, Y. Yin, M. Wang, S. Liu, S. Pang and X. Guo, Insights Into the Role of π-Electrons of Aromatic Aldehydes in Passivating Perovskite Defects, *Angew. Chem., Int. Ed.*, 2025, **64**, e202420369.

32 S. Teale, M. Degani, B. Chen, E. H. Sargent and G. Grancini, Molecular cation and lowdimensional perovskite surface

passivation in perovskite solar cells, *Nat. Energy*, 2024, **9**, 779–792.
33 Y. Du, J. Wu, X. Zhang, Q. Zhu, M. Zhang, X. Liu, Y. Zou, S. Wang and W. Sun, Surface passivation using pyridinium iodide for highly efficient planar perovskite solar cells, *J. Energy Chem.*, 2021, **52**, 84–91.
34 B. Li, Q. Liu, J. Gong, S. Li, C. Zhang, D. Gao, Z. Chen, Z. Li, X. Wu, D. Zhao, Z. Yu, X. Li, Y. Wang, H. Lu, X. C. Zeng and Z. L. Zhu, Harnessing strong aromatic conjugation in low-dimensional perovskite heterojunctions for high-performance photovoltaic devices, *Nat. Commun.*, 2024, **15**, 2753.
35 A. E. Maughan, J. A. Kurzman and J. R. Neilson, Hybrid Inorganic-Organic Materials with an Optoelectronically Active Aromatic Cation: $(C_7H_7)_2SnI_6$ and $C_7H_7PbI_3$, *Inorg. Chem.*, 2015, **54**, 370–378.
36 I. W. H. Oswald, E. M. Mozur, I. P. Moseley, H. Ahn and J. R. Neilson, Hybrid ChargeTransfer Semiconductors: $(C_7H_7)SbI_4$, $(C_7H_7)BiI_4$, and Their Halide Congeners, *Inorg. Chem.*, 2019, **58**, 5818–5826.
37 Y. Shen, *et al.*, Strain regulation retards natural operation decay of perovskite solar cells, *Nature*, 2024, **635**, 882–889.
38 Q. Liu and W. Liang, Structure and property tunability in monolayer halide lead-free double hybrid perovskites: effects of Rashba and biaxial strain, *J. Mater. Chem. A*, 2019, **7**, 11487–11496.
39 Y. B. Lee, S. B. Cho and Y. C. Chung, Tunable Indirect to Direct Bandgap Transition of Monolayer Sc_2CO_2 by the Strain Effect, *ACS Appl. Mater. Interfaces*, 2014, **140**, 14724–14728.
40 Y. J. Sun, D. Wang and Z. G. Shuai, Indirect-to-Direct Bandgap Crossover in Few-Layer Transition Metal Dichalcogenides: A Theoretical Prediction, *J. Phys. Chem. C*, 2016, **120**, 21866–21870.
41 W. P. Xu, J. Z. Zhao and H. Xu, Adsorption Induced Indirect-to-Direct Bandgap Transition in Monolayer Blue Phosphorus, *J. Phys. Chem. C*, 2018, **122**, 15792–15798.
42 Q. Tu, I. Spanopoulos, S. Hao, C. Wolverton, M. G. Kanatzidis, G. S. Shekhawat and V. P. Dravid, Probing Strain-Induced Bandgap Modulation in 2D Hybrid Organic–Inorganic Perovskites, *ACS Energy Lett.*, 2019, **4**, 796–802.
43 Zi-A. Nan, *et al.*, Revealing phase evolution mechanism for stabilizing formamidinium-based lead halide perovskites by a key intermediate phase, *Chem*, 2021, **7**, 2513–2526.
44 G. Pilania and B. P. Uberuaga, Cation ordering and effect of biaxial strain in double perovskite $CsRbCaZnCl_6$, *J. Appl. Phys.*, 2015, **117**, 114103.
45 D. Liu, *et al.*, Strain relaxation in halide perovskites *via* 2D/3D perovskite heterojunction formation, *Sci. Adv.*, 2025, **11**, eadu3459.
46 Q. Cheng, B. Wang, G. Huang, Y. Li, X. Li, J. Chen, S. Yue, K. Li, H. Zhang, Y. Zhang and H. Zhou, Impact of Strain Relaxation on 2D Ruddlesden–Popper Perovskite Solar Cells, *Angew. Chem., Int. Ed.*, 2022, **61**, e202208264.
47 Q. Li, Y. Zheng, H. Wang, X. Liu, M. Lin, X. Sui, X. Leng, D. Liu, Z. Wei, M. Song, D. Li, H. G. Yang, S. Yang and Y. Hou, Graphene-polymer reinforcement of perovskite lattices for durable solar cells, *Science*, 2025, **387**, 1069–1077.
48 Q. Liu, M.-G. Ju and X. C. Zeng, Unconventional perovskite-to-perovskite tandem cell designed by stacking with large-gap phosphonium-based analogs, *Mater. Today Energy*, 2024, **42**, 101556.
49 G. Kresse, Ab-Initio Molecular-Dynamics for Liquid-Metals, *J. Non-Cryst. Solids*, 1995, **193**, 222–229.
50 P. E. Blöchl, Projector Augmented-Wave Method, *Phys. Rev. B*, 1994, **50**, 17953–17979.
51 J. P. Perdew, K. Burke and M. Ernzerhof, Generalized Gradient Approximation Made Simple, *Phys. Rev. Lett.*, 1996, **77**, 3865–3868.
52 S. Grimme, Semiempirical GGA-type density functional constructed with a long-range dispersion correction, *J. Comb. Chem.*, 2006, **27**, 1787–1799.
53 S. Grimme, J. Antony, S. Ehrlich and H. Krieg, A consistent and accurate *ab initio* parametrization of density functional dispersion correction (DFT-D) for the 94 elements H-Pu, *J. Chem. Phys.*, 2010, **132**, 154104.
54 J. Moellmann and S. Grimme, DFT-D3 Study of Some Molecular Crystals, *J. Phys. Chem. C*, 2014, **118**, 7615–7621.
55 P. V. R. Schleyer, A. Maerker, A. Dransfeld, H. Jiao and N. J. R. van Eikema Hommes, Nucleus-Independent Chemical Shifts: A Simple and Efficient Aromaticity Probe, *J. Am. Chem. Soc.*, 1996, **118**, 6317–6318.
56 P. V. R. Schleyer, *et al.*, Nucleus-Independent Chemical Shifts (NICS) as an Aromaticity Criterion, *Chem. Rev.*, 2005, **105**, 3842–3888.
57 H. Jiao, *et al.*, Aromaticity and Antiaromaticity in Five-Membered C_4H_4X Ring Systems, *Angew. Chem., Int. Ed.*, 1997, **36**, 976–978.
58 F. Neese, The SHARK Integral Generation and Digestion System, *J. Comb. Chem.*, 2022, **44**, 381.
59 F. Neese, The ORCA program system, *Wiley Interdiscip. Rev. Comput. Mol. Sci.*, 2012, **2**, 73–78.
60 F. Neese, Software update: the ORCA program system, version 4.0, *Wiley Interdiscip. Rev. Comput. Mol. Sci.*, 2018, **8**, 1–6.
61 F. Neese, F. Wennmohs, U. Becker and C. Riplinger, The ORCA quantum chemistry program package, *J. Chem. Phys.*, 2020, **152**, 224108.
62 F. Neese, Software update: The ORCA program system—Version 5.0, *Wiley Interdiscip. Rev. Comput. Mol. Sci.*, 2022, **12**, e1606.
63 F. Neese, Approximate second-order SCF convergence for spin unrestricted wavefunctions, *Chem. Phys. Lett.*, 2000, **325**, 93–98.
64 A. D. Becke, Density-functional thermochemistry. III. The role of exact exchange, *J. Chem. Phys.*, 1993, **98**, 5648.
65 R. Ditchfield, Self-consistent perturbation theory of diamagnetism, *Mol. Phys.*, 1974, **27**, 789.
66 F. Weigend and R. Ahlrichs, Balanced basis sets of split valence, triple zeta valence and quadruple zeta valence quality for H to Rn: Design and assessment of second and third row, *Phys. Chem. Chem. Phys.*, 2005, **7**, 3297.

67 W. G. Spitzer and H. Y. Fan, Determination of Optical Constants and Carrier Effective Mass of Semiconductors, *Phys. Rev.*, 1957, **106**, 882–890.

68 P. Peksa, A. Maufort, M. Baranowski, A. Surrente, L. Lutsen, P. Plochocka, W. T. M. Van Gompel and M. Dyksik, Engineering the Effective Mass in 2D Perovskites *via* Octahedral Distortion, *J. Phys. Chem. C*, 2024, **128**, 17984–17989.

69 W. Yu, Y. Zou, H. Wang, S. Qi, C. Wu, X. Guo, Y. Liu, Z. Chen, B. Qu and L. Xiao, Breaking the bottleneck of lead-free perovskite solar cells through dimensionality modulation, *Chem. Soc. Rev.*, 2024, **53**, 1769–1788.

70 M. G. Ju, G. X. Sun, Y. Zhao and W. Z. Liang, A Computational View of the Change in the Geometric and Electronic Properties of Perovskites Caused by the Partial Substitution of Pb by Sn, *Phys. Chem. Chem. Phys.*, 2015, **17**, 17679–17687.

71 J. Feng and B. Xiao, Effective Masses and Electronic and Optical Properties of Nontoxic $MASnX_3$ (X = Cl, Br, and I) Perovskite Structures as Solar Cell Absorber: A Theoretical Study Using HSE06, *J. Phys. Chem. C*, 2014, **118**, 19655–19660.

72 L. Zhang and W. Z. Liang, How the Structures and Properties of Two-Dimensional Layered Perovskites $MAPbI_3$ and $CsPbI_3$ Vary with the Number of Layers, *J. Phys. Chem. Lett.*, 2017, **8**, 1517–1523.